Supporting Information

Laser-Induced Graphene-Based Corrugated Bimodal Sensor for Strain and Contact Monitoring in Wearables and Intelligent Robotics

Weixiong Yang [a, 1], Lingxue Ouyang [a, 1], Yuhan Guo [a, 1], Mingguang Han [a], Sida Luo [a, *]

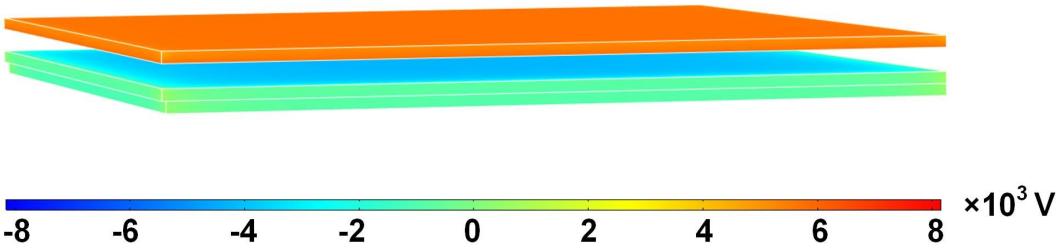

Figure S1. The distribution state of the electric potential field when an external object is at a medium distance.

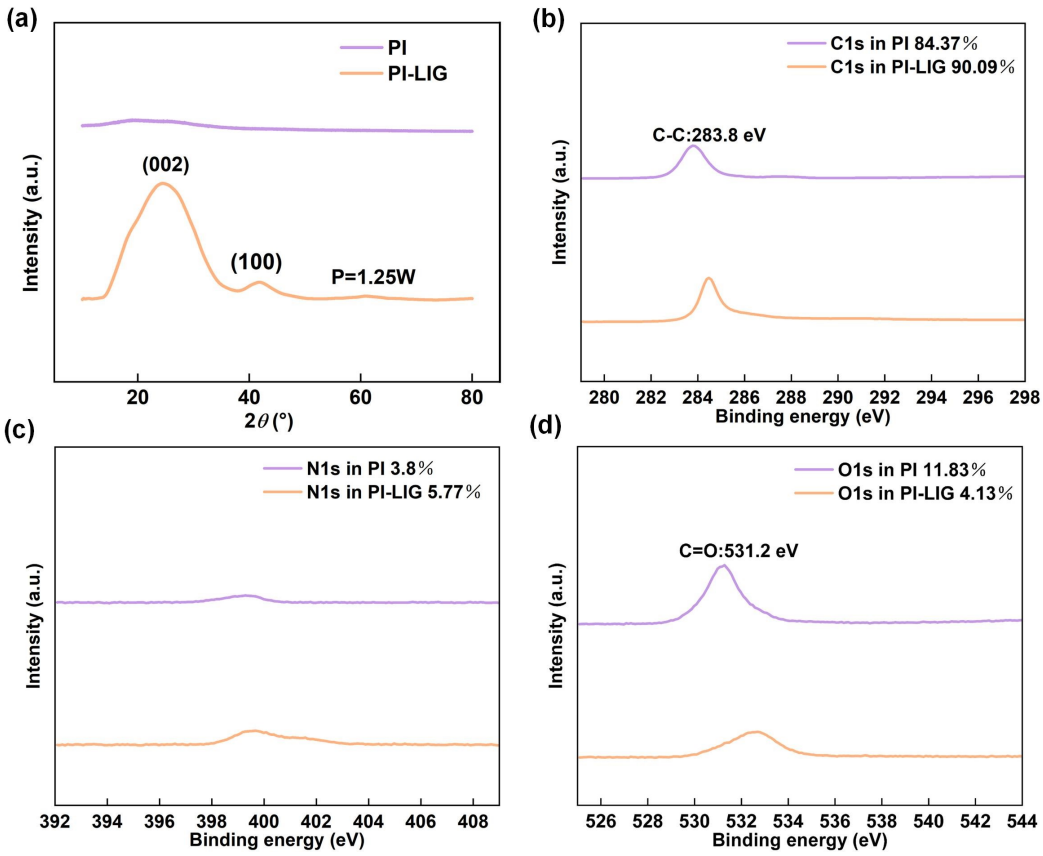

Figure S2. a XRD pattern of the original PI and LIG. **b** XPS pattern of C1s, **c** N1s and **d** O1s of the original PI and LIG.

XRD patterns in the Supporting Information further confirm the few-layer porous structure of the graphene electrode, with strong diffraction peaks corresponding to the (002) and (100) crystal planes appearing at 2θ = 25.1 and 2θ = 42.2, respectively (Fig. S2a). High resolution C1s XPS spectrum of the PI and LIG, showing the dominant C—C peak. High resolution O1s XPS spectrum of PI and LIG. High resolution N1s XPS spectrum of PI and LIG. The intensity of the O1s, N1s and F1s peak were greatly reduced after laser exposure.

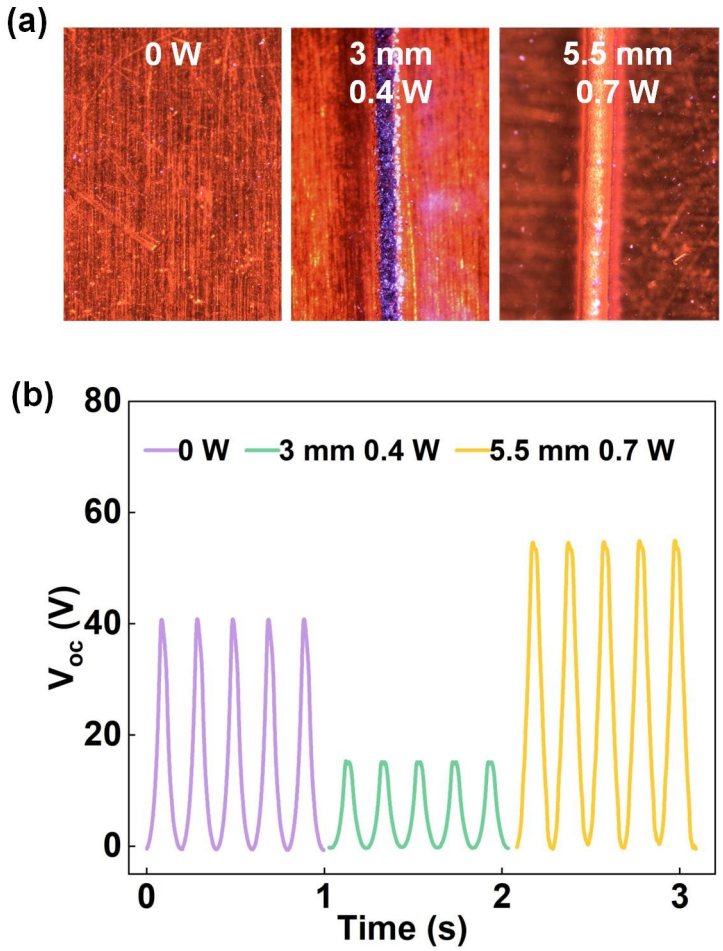

Figure S3. a Surface morphology and **b** Voltage performance comparison of pristine PI film, 3 mm focal length 0.4 W, and 5 mm focal length 0.7 W samples.

When the focal length is 3 mm, power of 0.4 W can carbonize the PI film, making the 3 mm focal length unsuitable for groove processing. Experimental test results show that with a focal length of 5.5 mm and a power of 0.7 W, the laser can fabricate a triboelectric nanogenerator (TENG) with the highest performance.

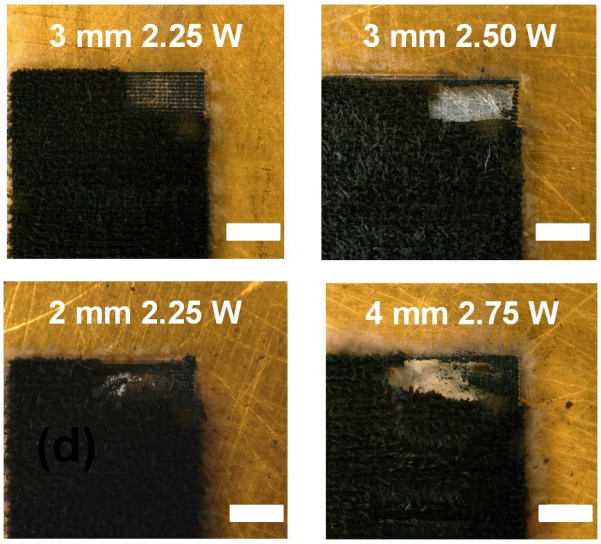

Figure S4. LIG fabricated under different powers and focal lengths (focal length 3 mm, power 2.25 W; focal length 3 mm, power 2.50 W; focal length 2 mm, power 2.25 W; focal length 4 mm, power 2.75 W).

The PI film was damaged under the following conditions: focal length 3 mm, power 2.50 W; focal length 2 mm, power 2.25 W; focal length 4 mm, power 2.75 W.

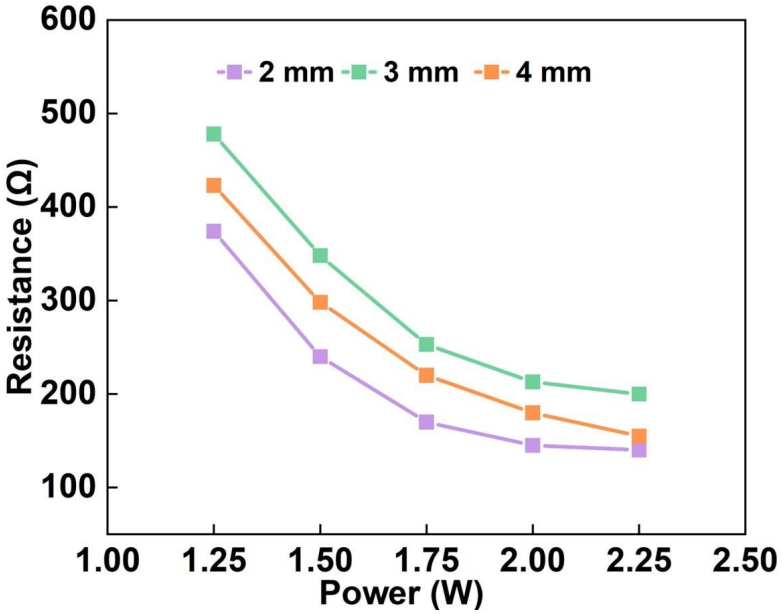

Figure S5. Comparison of sheet resistance of graphene electrodes under different processing conditions.

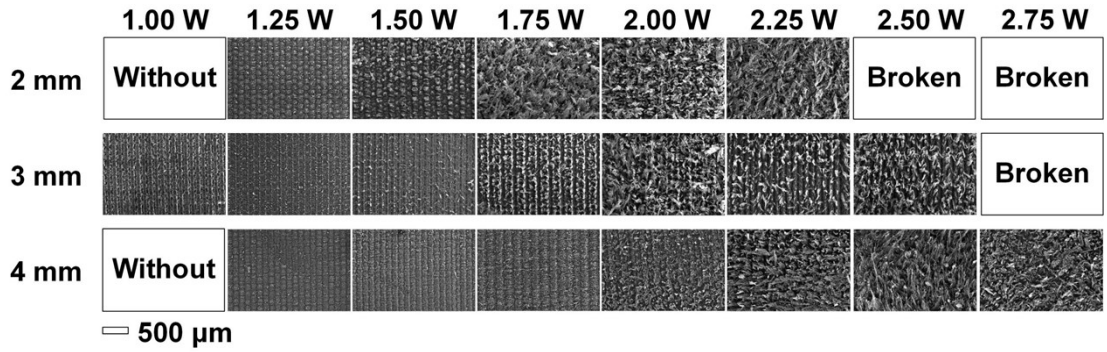

Figure S6. Surface morphology of the electrodes prepared with different powers and focal lengths.

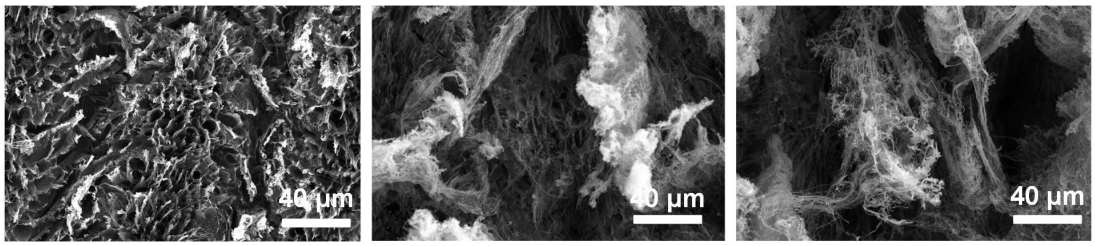

Figure S7. Pore structure of the electrodes prepared with different powers and focal lengths.

The focal length was fixed at 3 mm, and the applied powers were 1 W, 1.5 W, and 2.25 W, respectively. For the electrodes with a pore structure at the bottom, as the preparation power increases, more and more fibrous conductive networks appear on the top.

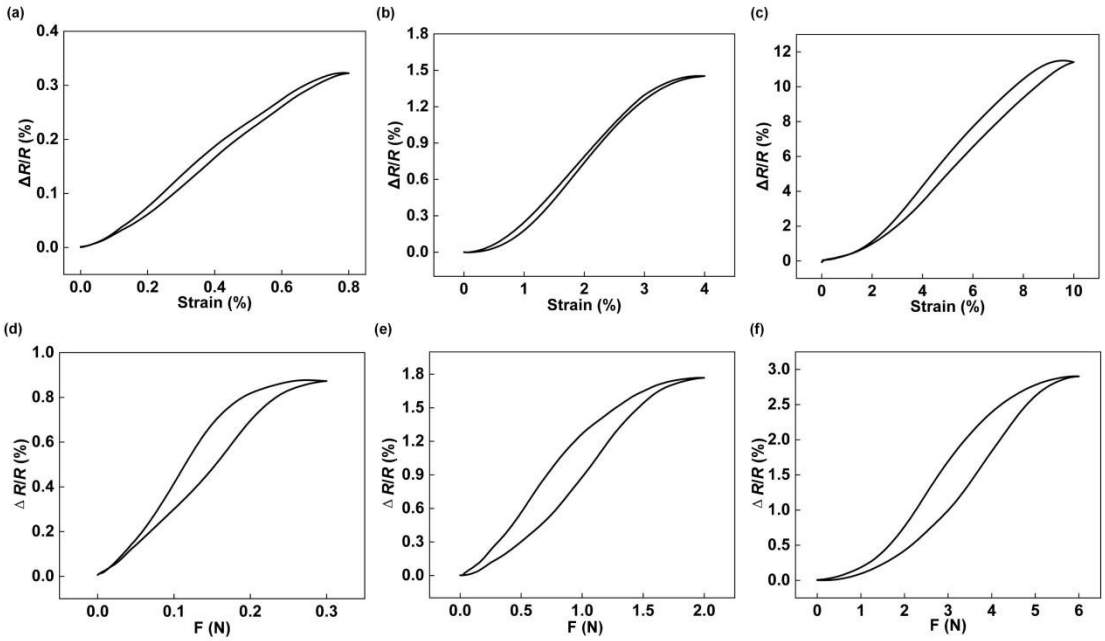

Figure S8. a-c Hysteresis loops of the strain unit under cyclic loading–unloading at 1%, 4%, and 10% strain. **d-f** Loading–unloading hysteresis loops of the strain unit under pressures of 0.3, 2, and 6 N.

Furthermore, we supplemented the hysteresis curves of the strain unit under tensile strains of 1%, 4%, and 10% (Figure S8a-c). The resistance returned to its initial value in each case, with no baseline drift observed. However, due to the inherent hysteresis of Ecoflex and the PI film, they do not instantly recover to their original length after the tensile force is released, leading to a discrepancy between the loading and unloading paths and thus giving rise to hysteresis. In addition, the graphene conductive network tends to reorganize under external stress, forming new conductive pathways. Upon unloading, the ruptured pathways cannot be restored instantaneously, and some newly formed pathways may persist, further contributing to the difference in resistance between the loading and unloading phases at the same strain. When the strain is below 4% (e.g., 1% and 4%), the calculated hysteresis errors (H) are 5.05% and 5.15%, respectively. However, when the strain exceeds 4% (e.g., 10%), the hysteresis error increases significantly to 10.40%. These values are within the normal range for flexible stretchable materials[1–5].

On the other hand, under pressure tests of 0.3, 2, and 6 N, the hysteresis error was larger than that observed in the tensile tests, reaching 22.83%, 25.28%, and 25.12%,

respectively (Figure S8d-f). This is attributed to the fact that, during pressure testing, the sensor was placed between two clamping plates. During the unloading process, the corrugated structure must overcome the frictional resistance from the clamping plates to recover, resulting in a delayed rebound of the corrugated architecture.

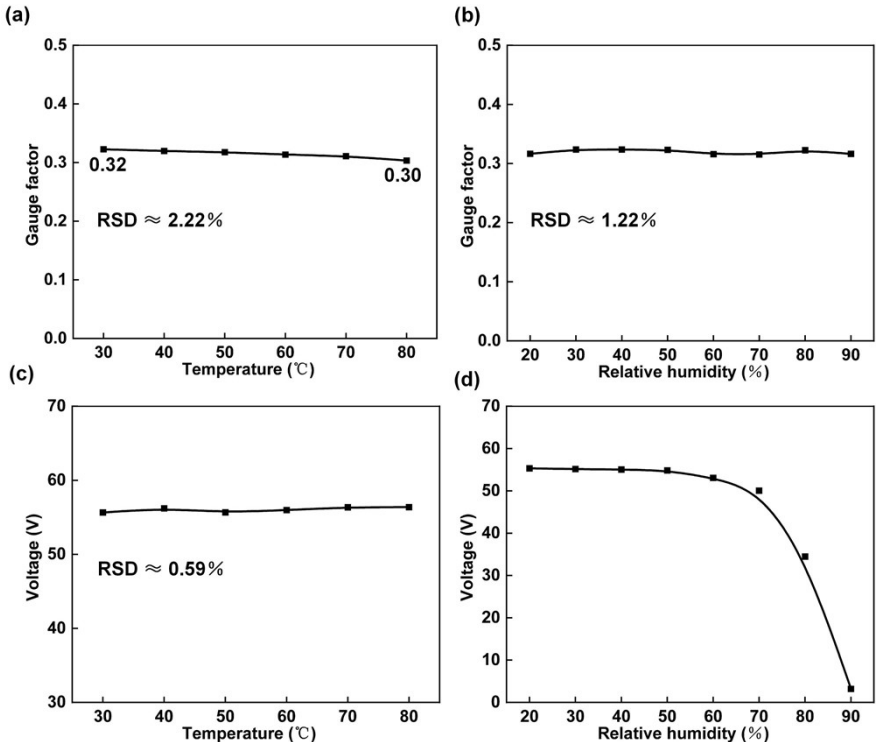

Figure S9. **a** Gauge factor (GF) of the strain unit at different temperatures. **b** GF of the strain unit at different humidity levels. **c** Performance of the triboelectric unit at different temperatures. **d** Performance of the triboelectric unit at different humidity levels.

All experiments in this work were conducted under ambient conditions with a temperature of approximately 20 °C and a relative humidity of about 20%. Furthermore, the performance of both the strain unit (at 3% strain) and the contact unit was evaluated under different temperature and humidity conditions. When the temperature increased from 30 °C to 80 °C, the gauge factor (GF) of the strain unit exhibited a very slight decrease (from 0.32 to 0.30), with a relative standard deviation (RSD) of approximately 2.20%. As the temperature rose, thermal expansion of Ecoflex caused the device to expand, leading to an increase in the baseline resistance (Figure S9a). When the relative humidity increased from 20% to 90%, the GF of the strain unit remained nearly unchanged (Figure S9b), with an RSD of only 1.22%. Because the graphene conductive network is encapsulated by Ecoflex, the strain unit is not affected by humidity variations.

As the temperature increased, the voltage output of the contact unit remained largely unaffected (Figure S9c), with an RSD of only 0.59%. When the relative

humidity exceeded 70%, the voltage output of the contact unit decreased significantly, with a further decrease observed at 90% relative humidity (Figure S9d). This degradation occurs because under excessively humid conditions, charge accumulation on the surface of the triboelectric material becomes difficult, leading to reduced triboelectric performance. Except for extremely humid environments, the sensor exhibits good adaptability and stability.

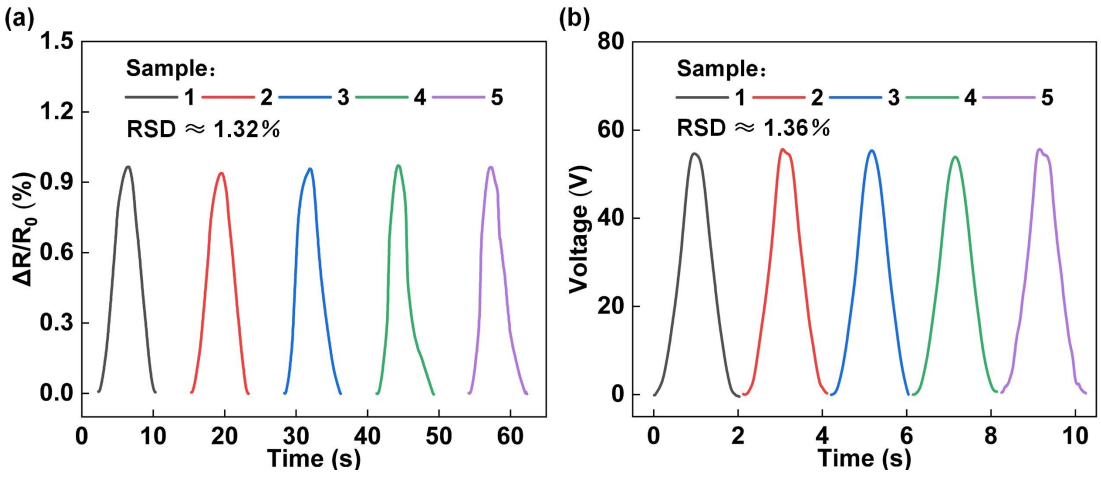

Figure S10. a Resistance change rate of different batches at 3% strain. **b** Performance of the contact unit across different batches.

To verify the stability and repeatability of corrugated bimodal sensor, we produced samples from five different batches and tested their stretch signals. The Figure S10a below shows the stretch signals of the five batches of samples at 3% strain. The ΔR/R0 values for the five samples are all around 0.95%, with a calculated relative standard deviation (RSD) of approximately 1.32%. Furthermore, the contact unit exhibited stable performance at approximately 55 V across different fabrication batches (Figure S10b), with a calculated RSD of approximately 1.36%. This low RSD value indicates excellent batch-to-batch consistency of the proposed sensor. These results collectively indicate that the proposed corrugated bimodal sensor possesses excellent stability and repeatability.

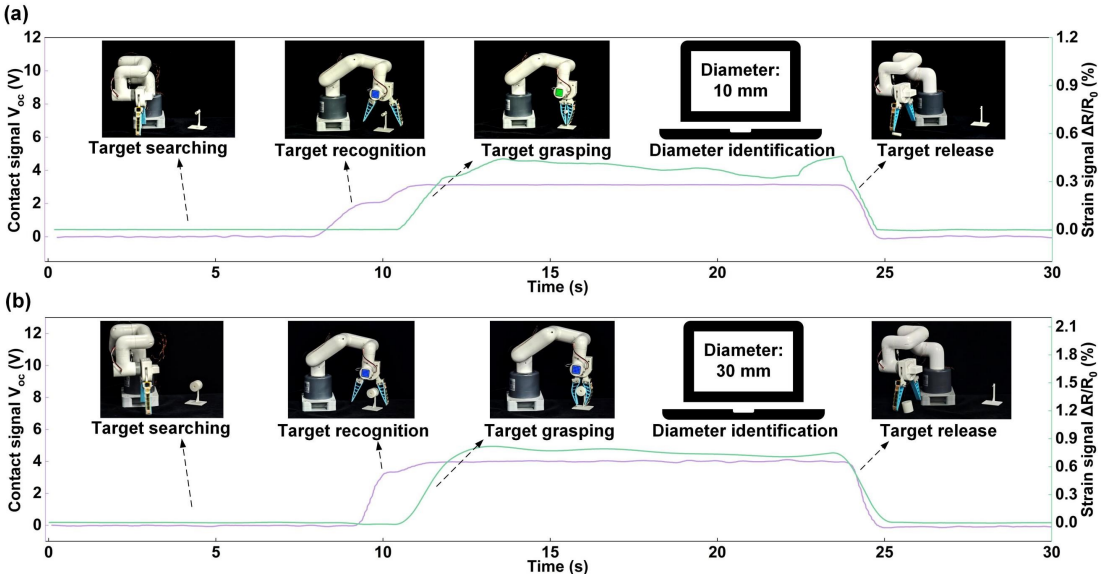

Figure S11. This intelligent robot is equipped with the CBS, which can autonomously locate, grasp, and identify target objects: **a** with a diameter of 10 mm, **b** with a diameter of 30 mm.

Table S1. Comparison of the performance and detection distance of the contact unit.

References	Area-normalized performance (V/cm^2)	Maximum detection distance (mm)
[6]	2.26	25
[7]	0.21	100
[8]	4	80
[9]	4	20
[10]	4.22	140
[11]	3.81	50
[12]	8	80
This work	24.4	100

The power generation capability of this work stands at a relatively excellent level compared to recently reported studies, benefiting from the microgroove structures fabricated by laser-induced graphene (Table S1).

Table S2. Comparison of fabrication steps, mumber of plies, gauge factor, and sensing range for recently reported flexible strain sensors.

References	Material type	Fabrication steps	Mumber of plies	Gauge factor	strain range (%)
[13]	Colloid	5	3	4.46	275
[14]	Colloid	4	2	3.07	50
[15]	Solid	3	6	1.7	20
[16]	Solid	4	4	4.18	1
[17]	Solid	5	5	1.3	7
[18]	Solid	2	2	0.15	10
[19]	Solid	5	2	5.2	5
This work	Solid	2	2	3.01	10

As compared in Table S2, leveraging the processing advantages of laser-induced graphene, the proposed sensor requires only one-step fabrication and one-step encapsulation, making both the processing steps and the number of device layers the most streamlined solution. While sensors with elastomeric substrates achieve high

stretchability, the proposed sensor, compared to other solid-substrate-based devices, exhibits excellent levels of both sensitivity and strain range. With its stretchability sufficient to meet application requirements, the highly integrated high-performance device with dual-sensing functionality greatly expands the application scenarios of the sensor.

References

1 Y. Qian, Y. Jin, Z. Gao, R. Guo, C. Sun, L. Chen and X. Zhou, *ACS Appl. Nano Mater.*, 2025, **8**, 19591–19597.

2 S. Lee, S.-H. Byun, C. Y. Kim, S. Cho, S. Park, J. Y. Sim and J.-W. Jeong, *Adv. Mater.*, 2022, **34**, 2204805.

3 S. Wu, S. Peng, Z. J. Han, H. Zhu and C. H. Wang, *ACS Appl. Mater. Interfaces*, 2018, **10**, 36312–36322.

4 S. Sharma and T. Mondal, *Small*, 2025, **21**, 2501722.

5 L. Cheng and J. Feng, *Chem. Eng. J.*, 2020, **398**, 125429.

6 W. Liu, Y. Duo, X. Chen, B. Chen, T. Bu, L. Li, J. Duan, Z. Zuo, Y. Wang, B. Fang, F. Sun, K. Xu, X. Ding, C. Zhang and L. Wen, *Adv. Funct. Mater.*, 2023, **33**, 2306368.

7 S. Peng, Y. Feng, Y. Liu, M. Feng, Z. Wu, J. Cheng, Z. Zhang, Y. Liu, R. Shen and D. Wang, *Nano Energy*, 2022, **104**, 107899.

8 G. Ye, Q. Wu, Y. Chen, X. Wang, Z. Xiang, J. Duan, Y. Wan and P. Yang, *Adv. Fiber Mater.*, 2024, **6**, 1874–1886.

9 W. Liu, Y. Duo, J. Liu, F. Yuan, L. Li, L. Li, G. Wang, B. Chen, S. Wang, H. Yang, Y. Liu, Y. Mo, Y. Wang, B. Fang, F. Sun, X. Ding, C. Zhang and L. Wen, *Nat. Commun.*, 2022, **13**, 5030.

10 K. Shrestha, S. Sharma, G. B. Pradhan, T. Bhatta, P. Maharjan, S. S. Rana, S. Lee, S. Seonu, Y. Shin and J. Y. Park, *Adv. Funct. Mater.*, 2022, **32**, 2113005.

11 F. Dong, Q. Peng, G.-A. Yu, H. Du, W. Sha, P. Li, Y. Liu, H. Cai, T. Du and M. Xu, *Small*, 2025, **21**, 2503393.

12 X. Li, P. Wang, C. Zong, H. Niu, P. Xu, Y. Yu, Y. Li and G. Shen, *Nano Energy*, 2025, **140**, 110995.

13 Y. Zhu, D. Yao, X. Gao, J. Chen, H. Wang, T. You, C. Lu and X. Pang, *ACS Appl. Mater. Interfaces*, 2024, **16**, 32466–32480.

14 J. Wu, Y. Liu, S. Hua, F. Meng, Q. Ma, S. Song and Y. Che, *ACS Appl. Mater. Interfaces*, 2023, **15**, 17293–17300.

15 T. Wang, X. Xu, S. Li, Y. Lan, K. Chen, W. Li, G. Wang, K. Yu, L. Sun and Y. Su, *Adv. Sci.*, 2025, e14779.

16 S. Y. On, S. Y. Park, W. Kim and S. S. Kim, *Compos. Sci. Technol.*, 2024, **251**, 110552.

17 Y. Kato, K. Fukuda, T. Someya and T. Yokota, *J. Mater. Chem. C*, 2023, **11**, 14070–14078.

18 A. Sinha, A. Sharma, P. Priyadarshi, A. Tulapurkar and B. Muralidharan, *Phys. Rev. Res.*, 2020, **2**, 043041.
19 Y. Jiang, Q. He, J. Cai, D. Shen, X. Hu and D. Zhang, *ACS Appl. Mater. Interfaces*, 2020, **12**, 58317–58325.